Frontiers in Heat and Mass Transfer

Tech Science Press

https://doi.org/10.32604/fhmt.2026.081154

ARTICLE

Enhancement of Thermal Performance of Heat Storage Tanks by the Synergistic Effect of Fin, Metal Foam, and Nanoparticles

Rukun Hu[1], Liao Zhang[1], Wenbin Han[1], Wei Chen[1], Bo Ma[1], Xuan Liu[1], Yongzhi Lei[1], Qian Lu[1], Yuanji Li[2] and Xiaohu Yang[2,*]

[1]Research Center of Energy Solution, PowerChina Northwest Engineering Corporation Limited, Xi'an, China
[2]Institute of the Building Environment & Sustainability Technology, School of Human Settlements and Civil Engineering, Xi'an Jiaotong University, Xi'an, China

*Corresponding Author: Xiaohu Yang. Email: xiaohuyang@xjtu.edu.cn

Received: 24 February 2026; Accepted: 30 March 2026; Published: 29 June 2026

ABSTRACT: To enhance the efficiency of phase change heat storage, this study investigates the synergistic effects and parameter interactions of a coupled strategy integrating fins, metal foam, and nanoparticles. A validated numerical model is developed for a shell-and-tube heat storage unit. The influence of porosity and pore density of metal foam, as well as Al_2O_3 nanoparticle concentration, on melting behavior, heat storage rate, and fluid flow features are systematically analyzed. Results indicate that reducing porosity significantly enhances heat conduction, shortening the complete melting time by up to 53.71%. Conversely, increasing pore density markedly suppresses natural convection, reducing the average liquid velocity by 64.62% and consequently extending the melting duration. The incorporation of nanoparticles consistently improves thermal performance; specifically, a 15% concentration reduces the melting time by 25.49%. Notably, a strong synergistic interaction is revealed. The enhancement of nanoparticles is more pronounced in metal foams with lower intrinsic conductivity, yielding an average additional enhancement of 17.24%. The optimal configuration identified in this study comprises metal foam with a porosity of 0.98 and a pore density of 10 PPI, coupled with 15% nanoparticles, achieving a heat storage rate 51.47% higher than the least efficient design. These findings elucidate the underlying coupling mechanisms and provide practical guidelines for the multi-parameter optimization of high-performance composite PCM-based thermal energy storage systems.

KEYWORDS: Melting characteristic; fin; metal foam; nanoparticles; latent heat storage; heat transfer enhancement

1 Introduction

The extensive combustion of fossil fuels has exacerbated the global energy crisis and led to severe environmental pollution [1]. Consequently, transitioning to renewable energy sources to replace fossil fuels has become a pivotal trend for future sustainable development [2,3]. However, the inherent intermittency and instability of clean energy sources pose significant challenges to stable energy supply [4,5]. Thermal energy storage (TES) has garnered considerable attention as an effective solution to address the temporal and spatial mismatches between energy supply and demand [6]. Conventional TES technologies are generally categorized into sensible heat storage, latent heat storage, and thermochemical storage [7,8]. Among these, Latent heat thermal energy storage (LHTES) utilizes phase change materials (PCMs) to absorb or release heat while maintaining a nearly constant temperature, thereby enabling high-density energy storage [9]. Nevertheless, the intrinsically low thermal conductivity of most PCMs severely hinders heat transfer

efficiency [10]. To mitigate this limitation, various enhancement strategies have been proposed, focusing on expanding the heat transfer area and improving the heat transfer coefficient [11,12].

Extending the heat transfer surface area is a mature and widely adopted strategy for enhancing thermal performance in various engineering applications. For instance, Li et al. [13] demonstrated that double-grooved surfaces yield higher condensation heat transfer coefficients compared to single-grooved counterparts, while comparative studies between finned and plain tubes have confirmed significant improvements in heat transfer rates [14]. Although condensation phase change differs from solid-liquid phase change, the concept of designing grooved surface provides a promising solution to enhancing phase change process. In the context of LHTES, attaching fins remains one of the most effective methods to mitigate the low conductivity of Phase Change Materials PCMs [15,16]. Extensive research has focused on optimizing fin geometry and configuration [17,18]. Jaberi and Hossainpour [19] investigated a hybrid strategy replacing solid fins with porous ones, identifying fin position and porosity as critical parameters; specifically, replacing lower solid fins with porous ones reduced melting time by 21.2%, although decreased porosity tended to prolong the process. Numerical simulations by Kim et al. [20] highlighted the influence of fin inclination, revealing that an angle of −20° minimized melting time under specific boundary conditions. Similarly, Abdellatif et al. [21] reported that optimizing the number and thickness of L-shaped fins could reduce melting time by up to 86.6%. Innovative designs have also been explored, Ali Khan et al. [22] proposed an arc-fin structure, finding that slender fins with large semicircular arcs achieved the highest energy storage density and reduced melting time by 71.75% compared to conventional longitudinal fins. Furthermore, Tang et al. [23] optimized discontinuous vertical fins, determining that a configuration with 15 mm length, 54° bifurcation angle, and 10 periods shortened the melting duration by 21.17%.

Another primary approach involves improving the effective thermal conductivity of the PCM by incorporating high-conductivity additives, such as nanoparticles and porous media [24,25]. The enhancement efficiency generally correlates positively with the thermal conductivity of the added materials including nanoparticles or metal foams, and is limited between the upper and lower bounds formed by the parallel and series arrangements of the two materials, as reported in the literature [26]. The dispersion of nanoparticles has been extensively studied to enhance thermal conductivity [27,28], with particle type and concentration being key influencing factors [29,30]. Daneshazarian et al. [31] observed that adding 0.5 wt% graphene nanoplatelets to octadecane yielded the shortest melting time and maximum energy storage capacity. Comparative studies by Abdolahimoghadam and Rahimi [32] evaluated Cu, CuO, TiO_2, CNT, and GNP nanoparticles. It was concluded that GNP offered superior enhancement, reducing melting time by 56.43% at a 5 vol% fraction. Cost-effectiveness analyses by Sundriyal et al. [33] identified 2% Al_2O_3 concentration as optimal, achieving a 21% reduction in melting time. Piroozmand and Ahmadi [34] further corroborated the superiority of GNP over Al_2O_3. They argued that the strategy achieved a 78.1% reduction in melting time with a 3 vol% GNP loading. In addition, porous media have become an effective method for enhancing heat transfer due to their large specific surface area and high thermal conductivity [26,35]. Particularly, metal foams (MF) have emerged as a potent solution due to their high specific surface area and intrinsic thermal conductivity [36,37]. Experimental studies by Yao and Wu [38] indicated that lower porosity and higher pore density significantly boost heat transfer efficiency. Recent efforts have shifted towards structural optimization, such as gradient designs [39,40]. Zheng et al. [41] demonstrated that a 2D porosity-gradient MF could reduce melting time by 12.07% compared to uniform structures, with optimal performance at an aspect ratio of 2.5. Li et al. [42] utilized Taguchi and response surface methods to optimize gradient porosity and pore density. The results showed that the optimal structural parameters obtained through Taguchi method and response surface method increased the heat transfer rate by 14.61%. Filling strategy also plays a crucial role. Liu et al. [43] experimentally investigated the melting performance of PCM under

four different filling methods. Results showed that scheme with MF filled at bottom had the shortest melting time, confirming the optimal filling strategy. Cheong et al. [44] explored the thermal performance of PCM under five MF filling shapes and optimized the vertical shape for LHTES tank. Additionally, Pourfallah and Languri [45] reported that copper MF (20 PPI) reduced melting time by 64%, noting that positive gradient configurations outperformed negative ones. Conical storage tanks filled with MF have also been examined to further enhance storage efficiency [46]. It was reported that the conical heat storage tanks with MF shaped the optimal geometry gains 16.01% faster thermal energy charging speed.

Beyond single-enhancement strategies, recent research has increasingly focused on the synergistic effects of coupled methods, particularly combinations of fins, metal foams, and nanoparticles [47,48]. Lu et al. [49] developed a fin-foam synergy technology, where numerical simulations of a triple-tube system with optimized fin distributions achieved a 59.7% reduction in charging time. Experimental work by Yang et al. [50] on composite PCMs (paraffin/MF/nanoparticles) revealed a 72.61% reduction in melting time compared to pure paraffin. Similarly, Yang et al. [51] designed a fin-MF integrated system that improved the heat storage rate by 36.52%. Heyhat et al. [52] comparatively analyzed fins, MFs, and nanoparticles, concluding that metal foams generally provide the most significant enhancement in phase change heat transfer.

Despite extensive investigations into individual and dual-enhancement strategies, a comprehensive understanding of the triplet coupling mechanism involving fins, metal foams, and nanoparticles remains elusive. Specifically, the interactive effects among these three components, i.e., how the intensity of one parameter influences the efficacy of the others, are not yet fully quantified. This knowledge gap significantly hinders the design of multi-parameter enhanced LHTES systems. To this end, this study systematically investigates the synergistic coupling of fins, metal foams, and nanoparticles. The individual and combined impacts of varying porosities, pore densities, and nanoparticle concentrations on melting behavior and heat storage rates are analyzed. The findings aim to elucidate the underlying coupling mechanisms and provide robust design guidelines for maximizing the performance of next-generation composite PCM-based thermal energy storage systems.

2 Model Display

2.1 Model Description

A shell-and-tube heat storage tank is designed and studied. The system comprises two concentric tubes with inner and outer diameters of 15 and 30 mm, respectively. Heat transfer fluid flows through the inner tube, while the PCM fills the annular space between the tubes. To enhance phase change heat transfer, aluminum fins were installed to create high-conductivity pathways within the tank. Subsequently, nickel MF were incorporated to establish a global conductive network. Finally, nanoparticles were dispersed into the PCM to further improve thermal performance. Fig. 1a illustrates the physical model of the proposed shell-and-tube storage unit. Fig. 1b,c depicts configurations with metal foams of different pore sizes (larger and smaller pores, respectively). Table 1 lists the thermophysical properties of the PCM, metal foams, and nanoparticles used in this study. Fig. 1d presents the computational domain and boundary conditions for the numerical simulation. Specifically, the inner wall is maintained at a constant temperature of 75°C, simulating the heat source. The outer boundary is set as adiabatic to represent perfect insulation. Perfect thermal contact is assumed at the interfaces between the fins, metal foams, and PCM. To evaluate the impact of design parameters on thermal performance, various configurations with different structural parameters were simulated. These designs are detailed in Table 2. The parameters investigated include porosity ranging from 0.980 to 0.995 (with intervals of 0.005), pore density in the range of 10, 20, and 30 PPI, and nanoparticle volume fraction of 0%, 5%, 10%, and 15%.

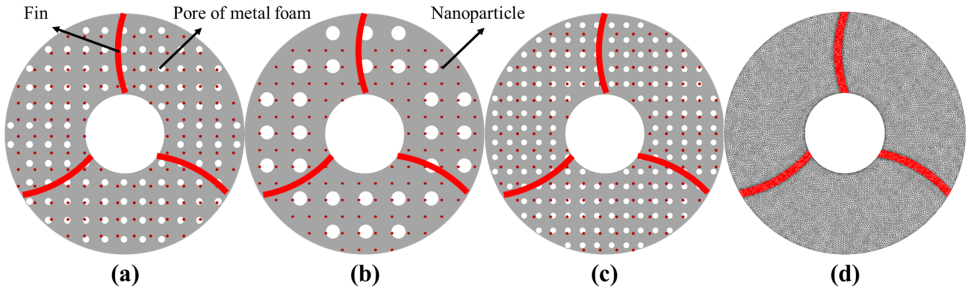

Figure 1: Display of heat storage with (**a**) middle pores, (**b**) larger pores, (**c**) lower pores and (**d**) numerical model.

Table 1: Thermophysical properties.

Parameters	Paraffin	Aluminum	Nickel	Al_2O_3 Nanoparticle	Unit
Density	785	2719	8907	3600	$kg \cdot m^{-3}$
Specific heat capacity	2850	871	460	765	$J \cdot kg^{-1} \cdot K^{-1}$
Thermal conductivity	0.2/0.1	202.4	91.7	36	$W \cdot m^{-1} \cdot K^{-1}$
Melting temperature	50–55				°C
Latent heat	102.1				$kJ \cdot kg^{-1}$
Kinematic viscosity	3.65×10^{-3}				$m^2 \cdot s^1$
Thermal expansion coefficient	3.09×10^{-4}			7.8×10^{-6}	K^{-1}

Table 2: Case matrix in this study.

Porosity	Pore Density	Nanoparticle Concentration	Porosity	Pore Density	Nanoparticle Concentration
0.980	10	0%	0.990	10	0%
		5%			5%
		10%			10%
		15%			15%
	20	0%		20	0%
		5%			5%
		10%			10%
		15%			15%
	30	0%		30	0%
		5%			5%
		10%			10%
		15%			15%
	10	0%		10	0%
		5%			5%
		10%			10%
		15%			15%

(Continued)

Table 2 (continued)

Porosity	Pore Density	Nanoparticle Concentration	Porosity	Pore Density	Nanoparticle Concentration
0.985	20	0%	0.995	20	0%
		5%			5%
		10%			10%
		15%			15%
	30	0%		30	0%
		5%			5%
		10%			10%
		15%			15%

2.2 Mathematical Model

The thermal transport in the designed composite system follows a hierarchical pathway: heat is first efficiently conducted via the high-conductivity fins; then distributed throughout the volume by the metal foam skeleton; and ultimately transferred to the nanoparticle-enhanced PCM matrix. Specifically, the heat transfer mechanism within the fins is purely conductive, described by the governing diffusion equation:

$$\rho c_p \frac{\partial T}{\partial t} = \lambda \left(\frac{\partial^2 T}{\partial x^2} + \frac{\partial^2 T}{\partial y^2} \right) \tag{1}$$

To characterize heat transfer within the porous metal foam, the volume averaging theory is utilized to formulate the macroscopic transport phenomenon. The mathematical formulation for the solid-liquid phase change process is given by:

Continuity equation:

$$\frac{\partial \langle u \rangle}{\partial x} + \frac{\partial \langle v \rangle}{\partial y} = 0 \tag{2}$$

Momentum equation:

$$\frac{\rho_f}{\varphi} \frac{\partial \langle u \rangle}{\partial t} + \frac{\rho_f}{\varphi^2} \left(\langle u \rangle \frac{\partial \langle u \rangle}{\partial x} + \langle v \rangle \frac{\partial \langle u \rangle}{\partial y} \right) = -\frac{\partial \langle P \rangle}{\partial x} + \frac{\mu_f}{\varphi} \left(\frac{\partial^2 \langle u \rangle}{\partial x^2} + \frac{\partial^2 \langle u \rangle}{\partial y^2} \right) - \left(\frac{\mu_f}{K} + \frac{\rho_f C_E}{\sqrt{K}} \left| \vec{U} \right| \right) \langle u \rangle - \frac{(1 - f_m)^2}{{f_m}^3 + \chi} \psi \langle u \rangle \tag{3}$$

$$\frac{\rho_f}{\varphi} \frac{\partial \langle v \rangle}{\partial t} + \frac{\rho_f}{\varphi^2} \left(\langle u \rangle \frac{\partial \langle v \rangle}{\partial x} + \langle v \rangle \frac{\partial \langle v \rangle}{\partial y} \right) = -\frac{\partial \langle P \rangle}{\partial y} + \frac{\mu_f}{\varphi} \left(\frac{\partial^2 \langle v \rangle}{\partial x^2} + \frac{\partial^2 \langle v \rangle}{\partial y^2} \right) - \left(\frac{\mu_f}{K} + \frac{\rho_f C_E}{\sqrt{K}} \left| \vec{U} \right| \right) \langle v \rangle - \frac{(1 - f_m)^2}{{f_m}^3 + \chi} \psi \langle v \rangle + \rho_f g \beta \left(\langle T_f \rangle - T_{m1} \right) \tag{4}$$

where f_m and φ are the volumetric melting fraction and melting fraction in pores of metal foam. ψ indicates the mushy coefficient, taken as 10^5 [53]. For permeability and inertia coefficient of MF, the calculation formulas are [54,55]:

$$K = 0.00073 d_p^2 (1 - \varepsilon)^{-0.224} \left(d_f / d_p \right)^{-1.11} \tag{5}$$

$$C_{\mathrm{E}}=0.095\frac{c_{\mathrm{d}}}{12}\sqrt{\frac{\varepsilon\left(1-(1-\varepsilon)^{1/3}\right)}{3(1-\varepsilon)\left((1-\varepsilon)^{-2/3}-1\right)}}\left(1.18\sqrt{\frac{1-\varepsilon}{3\pi}}\frac{1}{1-(1/e)^{\frac{1-\varepsilon}{0.04}}}\right)^{-1} \tag{6}$$

where d_{f} is the fiber diameter, which is calculated by $d_{\mathrm{f}}/d_{\mathrm{p}}=1.18\sqrt{\frac{(1-\varepsilon)}{\pi}}\frac{1}{1-e^{-25(1-\varepsilon)}}$.

Heat transfer within MF involves complex interactions between the solid metal skeleton and the saturated PCM. Consequently, separate energy governing equations for the solid and fluid phases are presented as follows:

Energy equation of the MF:

$$(1-\varepsilon)\rho_{\mathrm{s}}c_{ps}\frac{\partial\langle T_{\mathrm{s}}\rangle}{\partial t}=k_{\mathrm{se}}\left(\frac{\partial^2\langle T_{\mathrm{s}}\rangle}{\partial x^2}+\frac{\partial^2\langle T_{\mathrm{s}}\rangle}{\partial y^2}\right)-h_{\mathrm{sf}}a_{\mathrm{sf}}\left(\langle T_{\mathrm{s}}\rangle-\langle T_{\mathrm{f}}\rangle\right) \tag{7}$$

Energy equation of the PCM:

$$\begin{aligned}&\varepsilon\rho_{\mathrm{f}}\left(c_{pf}+L\frac{\mathrm{d}f_{\mathrm{m}}}{\mathrm{d}t}\right)\frac{\partial\langle T_{\mathrm{f}}\rangle}{\partial t}+\rho_{\mathrm{f}}c_{pf}\left(\langle u\rangle\frac{\partial\langle T_{\mathrm{f}}\rangle}{\partial x}+\langle v\rangle\frac{\partial\langle T_{\mathrm{f}}\rangle}{\partial y}\right)\\&=(k_{\mathrm{fe}}+k_{\mathrm{td}})\left(\frac{\partial^2\langle T_{\mathrm{f}}\rangle}{\partial x^2}+\frac{\partial^2\langle T_{\mathrm{f}}\rangle}{\partial y^2}\right)-h_{\mathrm{sf}}a_{\mathrm{sf}}\left(\langle T_{\mathrm{f}}\rangle-\langle T_{\mathrm{s}}\rangle\right)\end{aligned} \tag{8}$$

To characterize the energy transfer within the PCM-saturated metal foam, the effective thermal conductivity (k_{e}) is introduced into the governing energy equation. The formulation for calculating effective thermal conductivity, based on established models [56], is given as follows:

$$k_{\mathrm{e}}=\frac{\sqrt{2}}{2\left(R_{\mathrm{A}}+R_{\mathrm{B}}+R_{\mathrm{C}}+R_{\mathrm{D}}\right)} \tag{9}$$

$$R_{\mathrm{A}}=\frac{4d}{2\left(2e^2+\pi d(1-e)\right)k_{\mathrm{s}}+\left(4-2e^2-\pi d(1-e)\right)k_{\mathrm{f}}} \tag{10}$$

$$R_{\mathrm{B}}=\frac{(e-2d)^2}{(e-2d)e^2k_{\mathrm{s}}+\left(2e-4d-(e-2d)e^2\right)k_{\mathrm{f}}} \tag{11}$$

$$R_{\mathrm{C}}=\frac{\left(\sqrt{2}-2e\right)}{\sqrt{2}\pi d^2k_{\mathrm{s}}+\left(2-\sqrt{2}\pi d^2\right)k_{\mathrm{f}}} \tag{12}$$

$$R_{\mathrm{D}}=\frac{2e}{e^2k_{\mathrm{s}}+(4-e^2)k_{\mathrm{f}}} \tag{13}$$

where $e=0.16$ and $d=\sqrt{\frac{\sqrt{2}(2-\frac{3\sqrt{2}}{4}e^3-2\varepsilon}{\pi(3-2\sqrt{2}e-e)}}$. Convection heat transfer coefficient h_{sf} and specific surface area a_{sf} between MF and phase change material are calculated by [57],

$$h_{\mathrm{sf}}=\begin{cases}\left(0.35+0.5\mathrm{Re}^{0.5}\right)k_f/d_f, & 0\le\mathrm{Re}\le1\\0.76\mathrm{Re}^{0.4}\,\mathrm{Pr}^{0.37}\,k_f/d_f, & 1<\mathrm{Re}\le40\\0.52\mathrm{Re}^{0.5}\,\mathrm{Pr}^{0.37}\,k_f/d_f, & 40<\mathrm{Re}\le1000\\0.26\mathrm{Re}^{0.6}\,\mathrm{Pr}^{0.37}\,k_f/d_f, & 1000<\mathrm{Re}\le20000\end{cases} \tag{14}$$

$$a_{sf} = \frac{1.18\omega}{0.0224}\sqrt{3\pi\left(1-\varepsilon\right)} \tag{15}$$

To further enhance heat transfer, nanoparticles are dispersed into the base fluid to form nanofluids. This addition significantly alters the thermophysical properties of the resulting mixture. The nanofluid density is calculated using the volume-weighted average model by:

$$\rho_{nf} = \left(1-\xi\right)\rho_f + \xi\rho_s \tag{16}$$

where ξ represents the nanoparticles concentration. Subsequently, the thermal expansion coefficient and specific heat capacity of nanofluid can be determined by

$$\left(\rho\beta\right)_{nf} = \left(1-\xi\right)\left(\rho\beta\right)_f + \xi\left(\rho\beta\right)_s \tag{17}$$

$$\left(\rho c_p\right)_{nf} = \left(1-\xi\right)\left(\rho c_p\right)_f + \xi\left(\rho c_p\right)_s \tag{18}$$

The incorporation of nanoparticles also significantly alters the viscosity of the nanofluid. The property is primarily governed by the volume fraction of the suspended particles, as described by

$$\mu_{nf} = \frac{\mu_f}{\left(1-\xi\right)^{2.5}} \tag{19}$$

The thermal conductivity of nanofluids depends on the conductivities of both the nanoparticles and the base fluid, as well as the nanoparticle volume fraction, as expressed in Eq. (20):

$$\frac{\left(k\right)_{nf0}}{k_f} = \frac{k_s + 2k_f - 2\xi\left(k_f - k_s\right)}{k_s + 2k_f + \xi\left(k_f - k_s\right)} \tag{20}$$

Furthermore, to accurately calculate the effective thermal conductivity, the thermal dispersion effect induced by fluid motion can be considered:

$$k_d = C\left(\rho c_p\right)_{nf}\sqrt{u^2+v^2}\xi d_p \tag{21}$$

Here, the empirical coefficient C is adopted from literature [58]. Consequently, the final effective thermal conductivity is formulated as $k_{eff} = k_d + k_{eff0}$. It is important to note that nanoparticle sedimentation and agglomeration are neglected in this simulation.

3 Numerical Model Setup and Verification

3.1 Solution Settings

The governing equations were solved using a pressure-based solver. The PRESTO! scheme was employed for pressure interpolation, while the SIMPLE algorithm was utilized to handle the pressure-velocity coupling. Spatial discretization of the gradients was performed using the least-squares cell-based method, and temporal discretization was achieved using the second-order upwind scheme. The convergence criteria were set to residuals of 10^{-6} for continuity and momentum equations, and 10^{-12} for the energy equation, respectively. In addition to the numerical schemes, the following physical assumptions were adopted: (1) the fluid is incompressible with temperature-independent properties; (2) buoyancy forces are modeled using the Boussinesq approximation; and (3) volume changes associated with the solid-liquid phase change are neglected. All simulations were conducted using the ANSYS 2021 platform.

3.2 Independence Verification

To ensure the reliability of the numerical results, grid and temporal discretization independence tests are performed prior to parametric study. Three computational grids with 23,466, 47,832, and 66,741 elements are evaluated. As illustrated in Fig. 2a, the melting fraction profiles under 47,832 elements converge closely with those of the finest mesh (66,741 cells). This indicates that further refinement yields marginal improvements at the expense of excessive computational cost. Similarly, Fig. 2b presents the time-step sensitivity analysis for intervals of 0.5, 0.2, and 0.05 s. The time step of 0.2 s is selected as it provides an optimal trade-off, delivering accuracy comparable to the shorter time step (0.05 s) with substantially higher efficiency. Based on these validations, all subsequent simulations are conducted using the grid of 47,832 cells and the time step of 0.2 s.

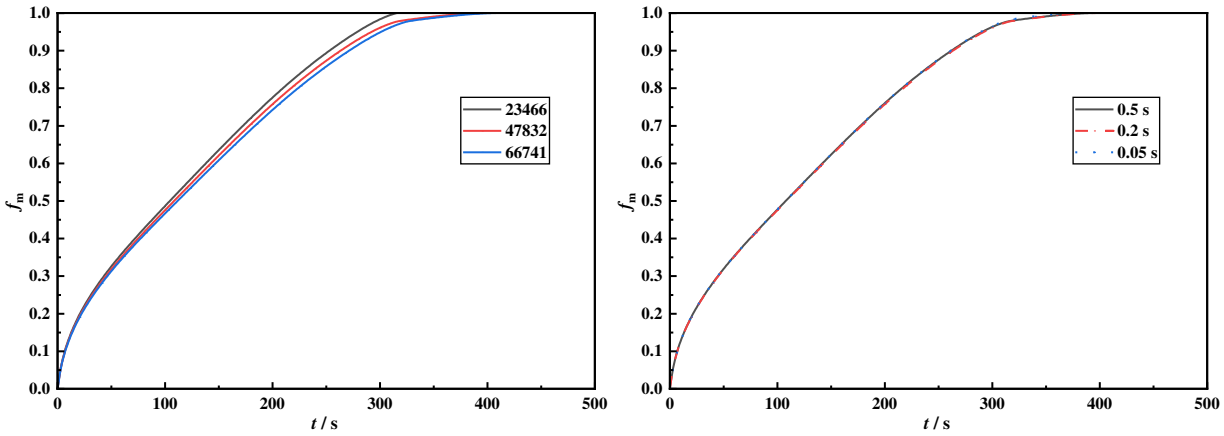

Figure 2: Comparison of melting fraction under different meshes (**a**) and different time steps (**b**).

3.3 Model Validation

3.3.1 Validation of Fin Enhanced Phase Change Heat Transfer Model

To verify the accuracy of the established numerical model, experimental and numerical data regarding solid-liquid phase change heat transfer in a finned thermal energy storage tank from literature [59] are utilized for comparison. In the reference, the system was initialized at 27°C and subsequently heated by a heat transfer fluid at 90°C with a flow rate of 8.3 L/min. The present numerical model is configured to replicate these exact operating conditions, and the comparative results are presented in Fig. 3. As shown, the predictions from the current model show excellent agreement with both the numerical simulations and experimental measurements reported in [59], thereby validating the accuracy of the proposed numerical framework.

3.3.2 Validation of Metal Foam Enhanced Phase Change Heat Transfer Model

Numerical validation is conducted for phase change heat transfer enhanced by MF, benchmarking against the experimental study [60]. The computational domain replicates a 100 mm × 100 mm × 30 mm rectangular enclosure containing a PCM with a melting range of 48.4°C–63.6°C and a latent heat of 148.8 kJ/kg. The system incorporates an MF matrix with a porosity of 0.95 and a pore density of 5 PPI. As illustrated in Fig. 4, the numerical results exhibit a similar variation trend with the experimental measurements. This close alignment confirms the fidelity and reliability of the proposed model in predicting MF-enhanced phase change process.

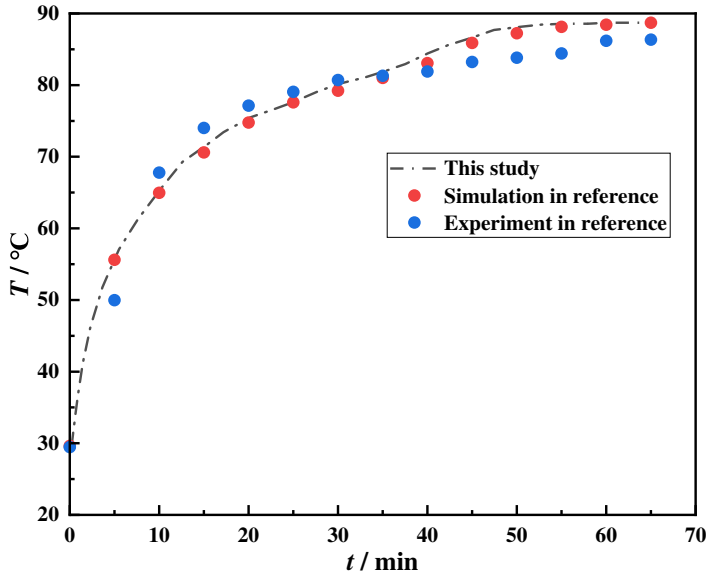

Figure 3: Comparison of simulation results and experimental results [59].

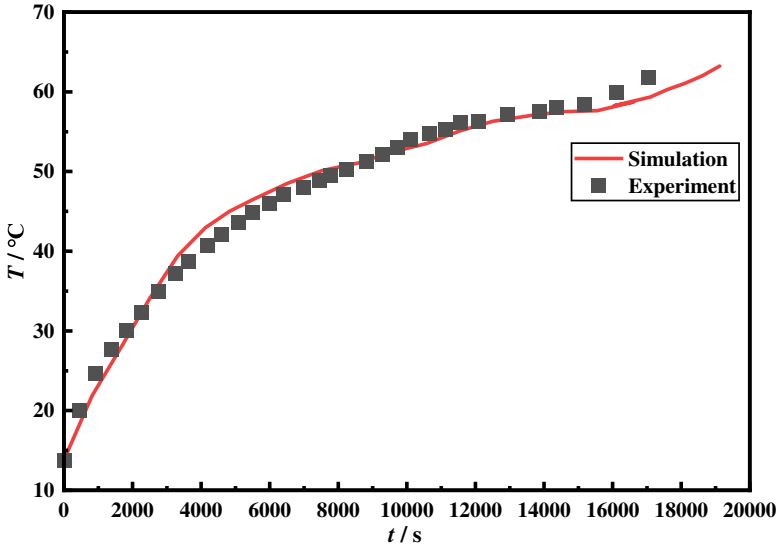

Figure 4: Comparison of simulation results and experimental results [60].

3.3.3 Validation of Nanoparticle Enhanced Phase Change Heat Transfer Model

To validate the numerical model for nanoparticle-enhanced phase change process, a case study involving a nanofluid with a 20 vol% nanoparticle concentration [61] is selected for replication. The established model is employed to simulate the transient liquid fraction evolution under these specific conditions. The numerical predictions are then compared with the reference data, as illustrated in Fig. 5. The results demonstrate an excellent agreement between the current simulation and the values in reference [61], thereby confirming the accuracy of the proposed numerical approach for modeling nano-enhanced phase change processes.

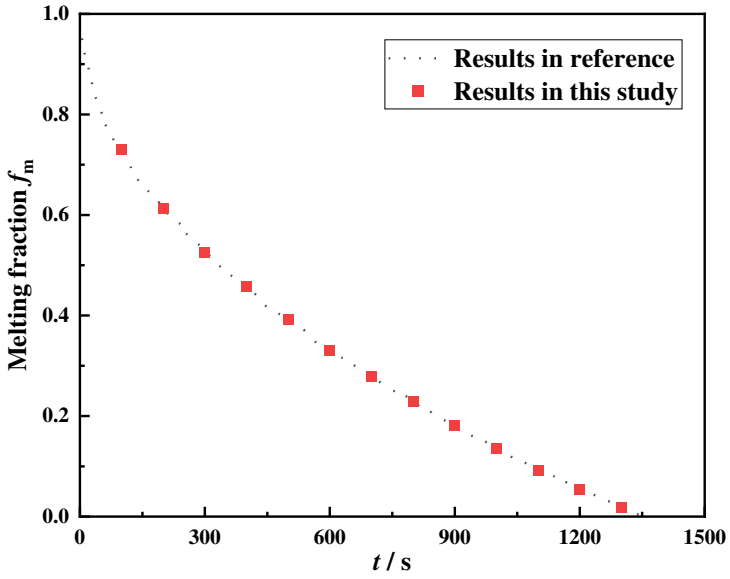

Figure 5: Comparison of simulation results and experimental results [61].

3.3.4 Validation of Metal Foam and Nanoparticle Enhanced Phase Change Heat Transfer Model

To validate the numerical model for phase change heat transfer enhanced by the synergistic effect of metal foams and nanoparticles, experimental results in reference [62] are selected for comparison. The reference study utilized a composite structure consisting of porous foam with a porosity of 0.98 embedded with 2 wt% graphite nanoparticles. Paraffin wax served as PCM with a melting point of 60°C. The system was initialized at 20°C and heated to a boundary temperature of 70°C. Fig. 6 compares the experimental data with the predictions from the current model. As shown, the proposed model accurately reproduces both the experimental measurements and numerical results reported in [62], thereby validating its accuracy in simulating hybrid-enhanced phase change processes.

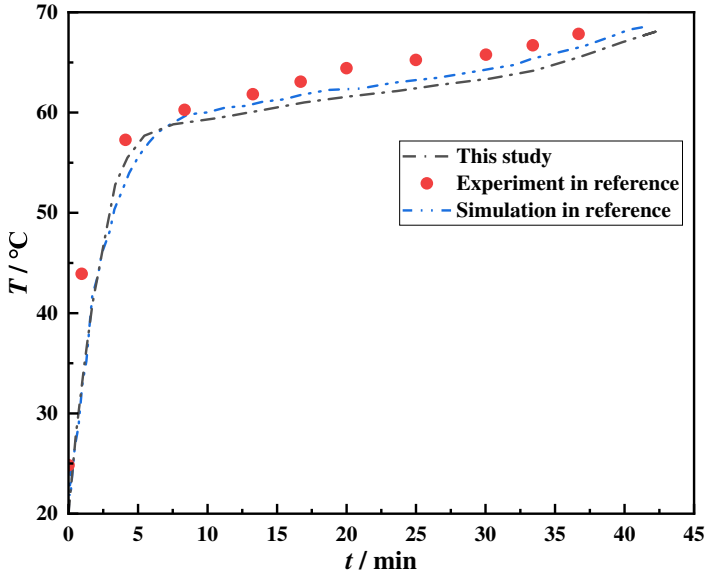

Figure 6: Comparison of simulation results and experimental results [62].

4 Results and Discussion

4.1 Comparison of the Enhancement

Fig. 7 compares the transient liquid fraction and total melting time for the thermal energy storage unit containing: pure PCM, fin, fin-foam composite, and fin-foam-nanoparticle hybrid structure. As shown in Fig. 7a, the pure PCM case exhibits the lowest liquid fraction evolution. The melting rate progressively accelerates with the incorporation of fins, metal foams, and nanoparticles. Consequently, the hybrid structure (fins + foam + nanoparticles) achieves the highest liquid fraction during the whole melting process. Fig. 7b quantitatively evaluates the total melting time and the corresponding heat transfer enhancement. The pure PCM requires 1986 s to fully melt. The addition of fins reduces this time to 913 s, representing a 54.03% reduction. Integrating metal foam further shortens the melting time to 553 s, increasing the total time savings to 72.16% relative to the pure PCM case, i.e., an additional 18.13% improvement over the fin-only scenario is achieved. Finally, dispersing 15 vol% nanoparticles into the matrix reduces the melting time to 412 s, yielding a total reduction of 79.25% (an additional 7.09%). This comparative analysis clearly demonstrates the synergistic heat transfer enhancement achieved by the sequential addition of fins, metal foams, and nanoparticles.

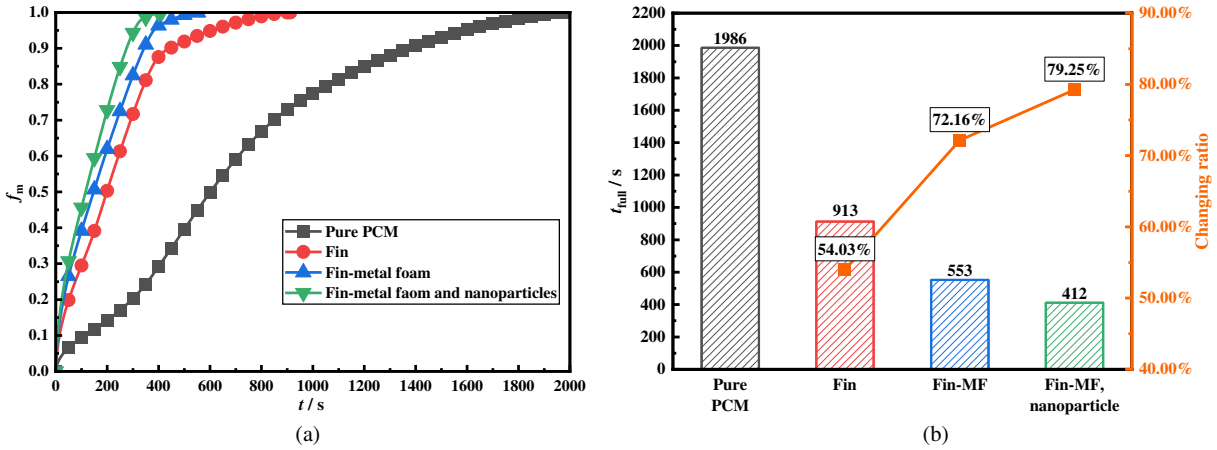

Figure 7: Comparison of the (**a**) transient melting fraction and (**b**) complete melting time for heat storage with pure PCM, fin, fin-metal foam, and fin-foam-nanoparticle hybrid.

4.2 Influence of Porosity

4.2.1 Transient Melting Fraction and Complete Melting Time

Fig. 8 depicts the influence of metal foam porosity on the transient liquid fraction and total melting duration. Fig. 8a reveals a clear inverse correlation between porosity and melting kinetics: systems with lower porosity exhibit markedly faster phase change rates. The configuration with $\varepsilon = 0.98$ demonstrates the most rapid melting progression. This behavior is driven by the enhanced effective thermal conductivity associated with a denser metal matrix (lower ε), which facilitates more efficient heat diffusion into the PCM. Notably, the discrepancies in liquid fraction among different porosities diverge progressively over time. This divergence stems from the cumulative effect of superior heat flux penetration in low-porosity foams, which sustains a larger driving temperature difference, thereby accelerating the melting front propagation relative to high-porosity cases. Quantitative analysis in Fig. 8b confirms these trends. The baseline case with high porosity ($\varepsilon = 0.995$) requires 553 s for complete melting. A reduction in porosity to 0.99 decreases this duration to 397 s, i.e., a 28.2% improvement. The most significant enhancement is observed at $\varepsilon = 0.98$, where the melting

time is minimized to 256 s, achieving a substantial 53.7% reduction relative to the one with a porosity of 0.995. These results underscore that optimizing metal foam porosity towards lower values is a highly effective strategy for intensifying heat transfer in latent heat storage systems, primarily by maximizing the conductive thermal pathway.

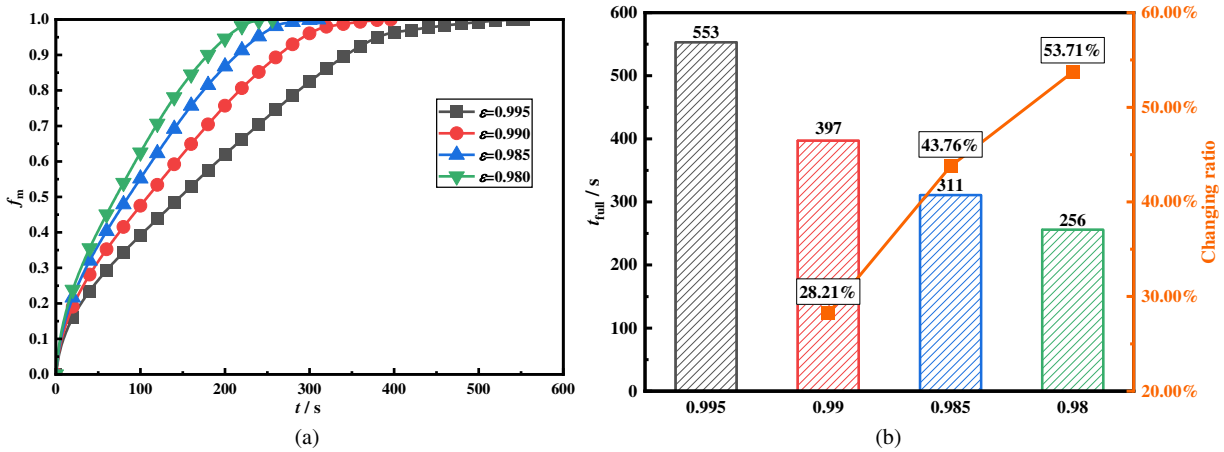

Figure 8: Comparison of the (**a**) melting fraction and (**b**) melting time for different porosity designs.

4.2.2 Melting Front

Fig. 9 compares the transient evolution of the melting interface in metal foams with varying porosities. At 50 s, no significant differences are observed among the cases, as the system has not yet developed distinct thermal gradients driven by the foam structure. However, by 100 s, the influence of porosity becomes apparent, and the disparities in the melting front morphology further widen at 150 s. For the high porosity case (ε = 0.995), the melting front in the upper region exhibits a highly distorted and curved profile. As porosity decreases, this curvature diminishes, resulting in a progressively flatter and more uniform interface. This phenomenon is attributed to the fact that lower porosity reduces the pore diameter, thereby increasing flow resistance and suppressing natural convection. Consequently, heat transfer shifts towards a conduction-dominated regime, which promotes a more uniform melting front. Specifically, in the case with ε = 0.995, the pronounced curvature is confined to the upper PCM region where natural convection is vigorous. In contrast, the region below the lower fins remains relatively flat because heat transfer there is primarily governed by conduction, with limited convective activity. By 200 s, substantial unmelted PCM remains in the case with a porosity of 0.995, whereas the case with ε = 0.98 has already achieved complete melting. This confirms that lower porosity facilitates more efficient heat diffusion, accelerating the phase change process. At 250 s, when the porosity takes a value of 0.98, the configuration is nearly fully melted, while significant solid regions persist in the one with ε = 0.995.

4.2.3 Temperature Distribution

Spatial temperature distribution provides insights into the underlying heat transfer dynamics. Fig. 10 illustrates the transient thermal contours across varying metal foam porosities, revealing the mechanism by which pore structure governs melting kinetics. At the early stage (50 s), notable deviations appear along the solid-liquid interface. Specifically, the low-porosity configuration displays a more extensive and uniform high-temperature zone, demonstrating its superior capacity to conduct heat across the phase boundary into the solid core. As the process evolves to 100 s, a stark contrast emerges: the PCM in low-porosity tanks uniformly exceeds 30°C, while substantial regions in the high-porosity tank (ε = 0.995) remain thermally

lagging (<30°C). This thermal homogenization in the low-porosity case is achieved much earlier, whereas the high-porosity system requires up to 200 s to elevate the entire domain above 30°C. By 250 s, the case with ε = 0.980 exhibits advanced thermal saturation in the upper region, approaching the heating source temperature, with only minimal solid remnants persisting at the bottom. Conversely, the high-porosity case still struggles with thermal uniformity. These results underscore that reducing porosity enhances effective thermal conductivity, thereby accelerating thermal propagation and ensuring a more rapid and uniform phase change process.

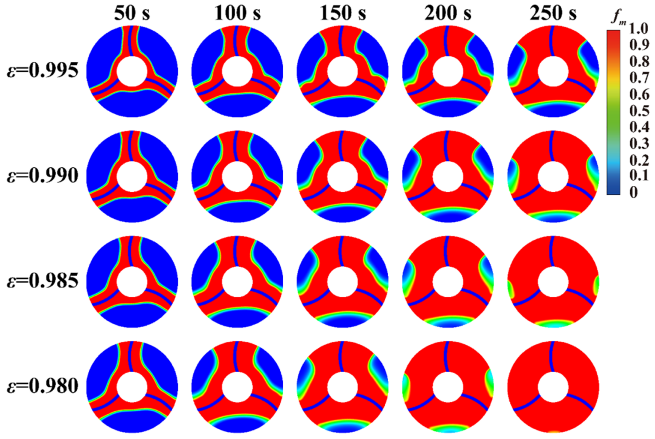

Figure 9: Comparison of melting front in LHTES with different porosity designs.

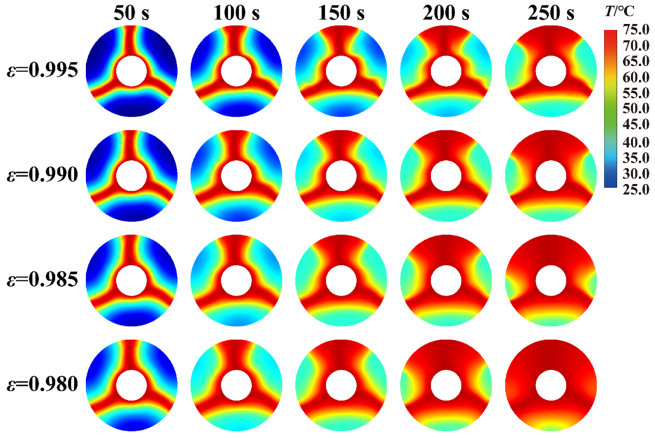

Figure 10: Comparison of the temperature distribution inside tank with different porosity designs.

4.3 The Influence of Pore Density

4.3.1 Transient Melting Fraction and Complete Melting Time

Fig. 11 illustrates the impact of metal foam pore density on the melting performance of the thermal energy storage unit. Fig. 11a depicts the transient liquid fraction for different PPI values. The configuration with 10 PPI consistently exhibits the highest liquid fraction throughout the process. Notably, the 20 PPI case outperforms the 30 PPI case. This trend is primarily attributed to the fact that increasing pore density reduces the pore size, thereby significantly increasing internal flow resistance. This heightened resistance strongly inhibits natural convection, which is a critical heat transfer mechanism during the melting phase. Fig. 11b

quantitatively compares the total melting times. The case with metal foam of 10 PPI achieves the shortest complete melting time of 553 s, whereas the one with 30 PPI requires the longest time of 596 s. Consequently, the higher pore density (30 PPI) results in a 7.78% increase in melting time compared to the optimal case (10 PPI). These results indicate that lower pore densities are more favorable for enhancing heat transfer by facilitating stronger natural convection currents.

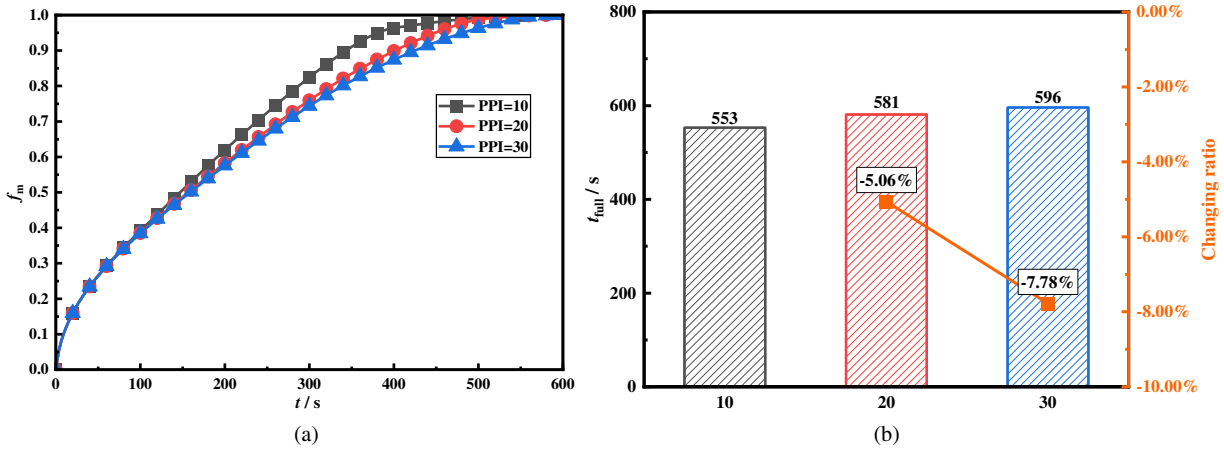

Figure 11: Comparison of transient (**a**) melting fraction and (**b**) melting time in tank with different pore density designs.

4.3.2 Melting Front and Streamline

To elucidate the effect of metal foam pore density on natural convection, Fig. 12 presents the evolution of phase interfaces and streamlines for different PPI configurations. Comparisons of the melting front contours and streamline distributions at 80, 160, and 240 s reveal that increasing pore density results in a progressively flatter melting front in the upper PCM region. This morphological change is attributed to the increased flow resistance caused by reduced pore sizes, which significantly weakens internal natural convection. The velocity contours in the figure further corroborate this mechanism. As pore density increases, the flow velocity of the liquid PCM markedly decreases. Specifically, the case with a pore density of 10 PPI exhibits high-velocity flow zones (indicated by red), whereas the 20 PPI case shows reduced velocities (green). At 30 PPI, the flow velocity is minimal, with the field dominated by low-velocity regions (blue). This suppression of natural convection leads to a noticeable lag in the melting progress of the upper PCM. By 320 s, the upper PCM in the tank with low pore density (10 PPI) has completely melted, whereas significant unmelted regions persist in the upper section of the tank with high pore density (30 PPI).

4.3.3 Average Velocity

While Fig. 12 qualitatively illustrates the streamline patterns at characteristic moments, Fig. 13 provides a quantitative comparison of the average fluid velocity to assess the impact of pore density on convective intensity. Fig. 13a depicts the evolution of the instantaneous average velocity. The 10 PPI configuration consistently exhibits the highest velocity throughout the melting process, whereas the 30 PPI case shows the lowest. Notably, the 10 PPI foam maintains a significantly stronger flow field compared to higher pore densities. Fig. 13b summarizes the time-averaged velocities over the entire melting duration. The 10 PPI tank achieves an average velocity of 0.05091 m/s. As the pore density increases to 20 PPI, the average velocity drops to 0.02965 m/s, representing a 41.76% reduction. A further increase to 30 PPI causes the velocity to decrease to 0.01801 m/s, corresponding to a substantial 64.62% decrease relative to the 10 PPI baseline. These

results quantitatively confirm that increasing pore density severely suppresses natural convection within the metal foam matrix.

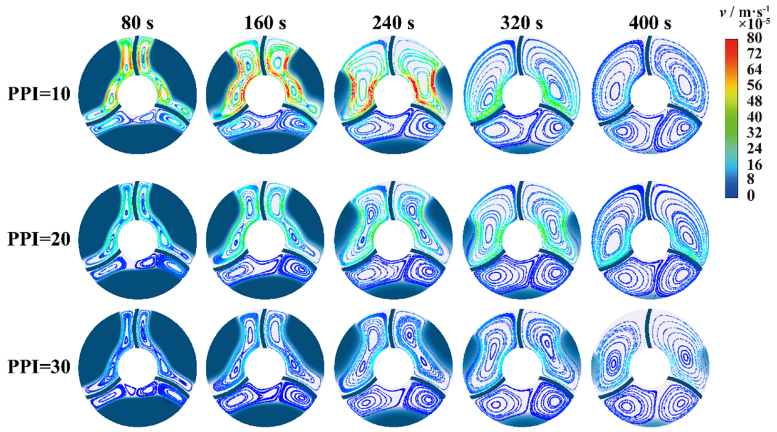

Figure 12: Comparison of complete melting front and streamlines under different pore density designs.

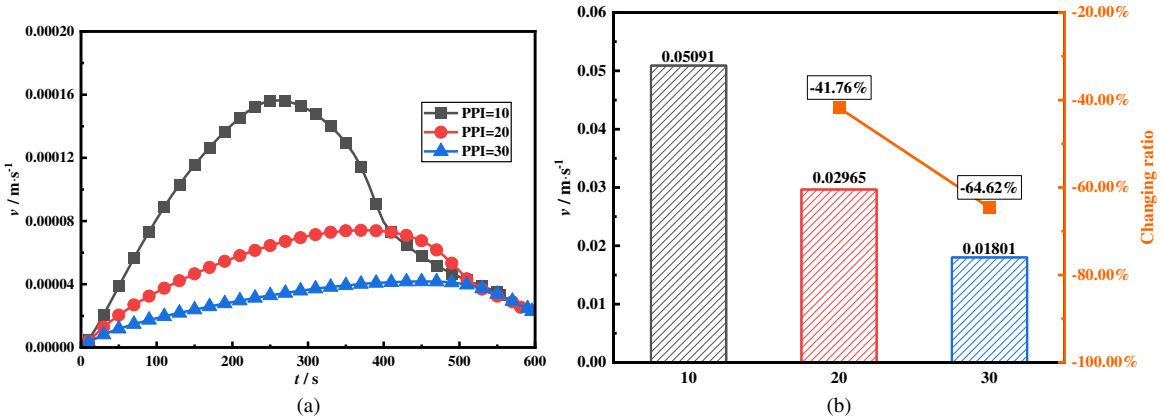

Figure 13: Comparison of (**a**) transient velocity and (**b**) integral average velocity under different pore density designs.

4.4 The Influence of Nanoparticle Concentration

Fig. 14 compares the transient liquid fraction for different nanoparticle concentrations. The results indicate a positive correlation: at any given time, higher nanoparticle concentrations yield higher liquid fractions. This enhancement is attributed to the increased effective thermal conductivity of the nanofluid-PCM hybrid, which accelerates heat diffusion during phase change. Within the concentration range studied (0%–15%), no decline in melting performance is observed. However, it is important to note that this trend is specific to the tested range. At significantly higher concentrations, the consequent rise in dynamic viscosity would suppress natural convection. If this convective inhibition outweighs the conductive enhancement, the overall melting rate would decrease. Fig. 15 presents the velocity contours, confirming that increasing nanoparticle concentration leads to a reduction in fluid velocity within the tank due to higher viscosity. Despite this, the net effect in this study remains positive. Fig. 14b quantifies the total melting time. The baseline case (0% nanoparticles) required 553 s. Adding 5% nanoparticles reduces the time to 505 s (an 8.68% reduction). Further increases to 10% and 15% shorten the melting time to 456 s (17.54% reduction) and

412 s (25.49% reduction), respectively. These results demonstrate that, within the investigated range, thermal conductivity enhancement dominates over the viscous damping of natural convection.

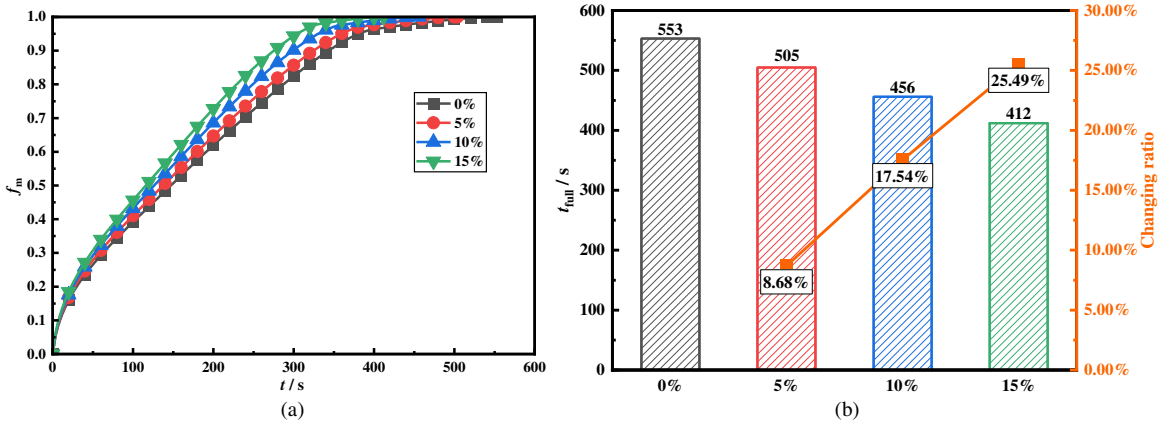

Figure 14: Comparison of (**a**) transient melting fraction and (**b**) melting time in tank with different nanoparticle concentrations.

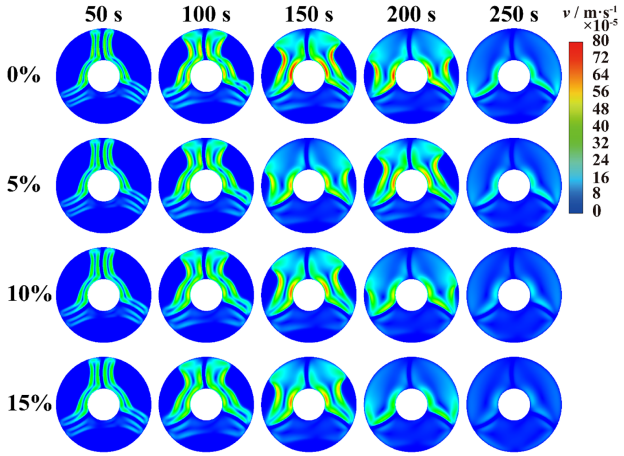

Figure 15: Comparison of velocity distribution under different nanoparticle additions.

4.5 The Interaction Effect of Metal Foams on the Filling of Nanoparticles

Fig. 16a compares the complete melting time under varying porosities and pore densities. The results show that increasing porosity leads to a longer melting time, primarily due to the reduced volume fraction of the high-conductivity metal matrix. However, the relative enhancement ratio provided by nanoparticles increases with porosity. Specifically, as porosity rises from 0.980 to 0.985 and 0.995, the average enhancement ratio increases from 10.54% to 11.90% and 17.24%, respectively. This trend occurs since higher porosity weakens the intrinsic heat conduction of the foam, the conductive bridge formed by nanoparticles becomes the decisive factor for heat diffusion. A similar synergistic mechanism operates with pore density. As pore density increases, natural convection is increasingly suppressed, shifting the dominant heat transfer mode towards conduction. Consequently, adding nanoparticles yields a greater marginal gain in high-PPI configurations. For 10 PPI, the average enhancement is 13.36%; this rises to 13.68% for 20 PPI and 14.08% for 30 PPI. The maximum enhancement (14.08%) is observed at the combination of highest porosity (0.995) and highest pore density (30 PPI), where both conduction and fluid convection are weakest, maximizing

the relative contribution of nanoparticle-enhanced conductivity. Fig. 16b illustrates the interaction effects of these three factors on melting time. Sensitivity analysis reveals that porosity exerts the most significant influence on the response, followed by nanoparticle concentration, while pore density has the relatively smallest impact.

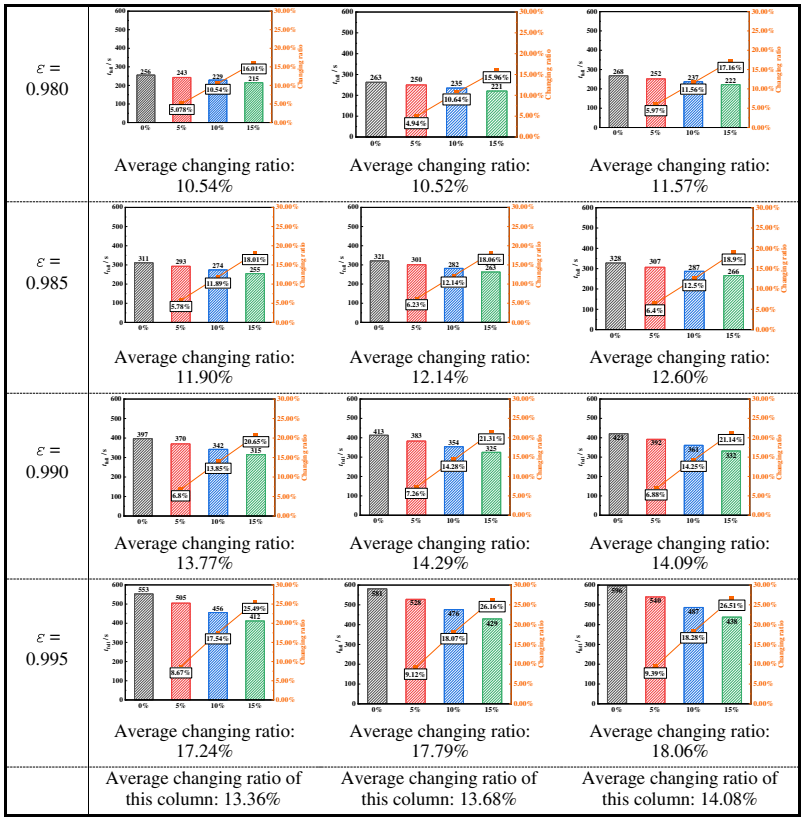

(a)

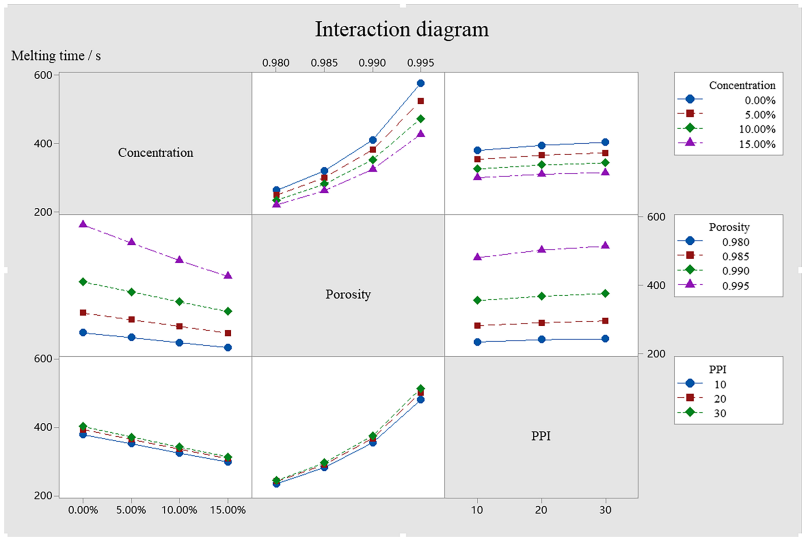

(b)

Figure 16: (**a**) Comparison of complete melting time and changing ratio under different porosities, pore densities and nanoparticle additions and (**b**) Interaction diagram.

4.6 The Heat Storage Characteristic

Heat storage capacity is a critical metric for evaluating thermal energy storage performance. This section conducts a comparative calculation and analysis of the total heat storage capacity and heat storage rate. The calculations are carried out using the following formulas respectively.

The total heat storage:

$$Q_{\text{total}}(t) = c_{pf} m \left(T_{\text{ave}}(t) - T_{\text{initial}}\right) + mLf_{\text{l}}(t) \tag{22}$$

The heat storage rate:

$$q_{\text{ave}} = \frac{Q_{\text{total}}(t_{\text{full}})}{t_{\text{full}}} \tag{23}$$

Fig. 17 compares the transient cumulative heat storage for metal foam tanks infused with 15% nanoparticles. The results indicate that at any given time, the configuration with 0.980 porosity achieves the highest heat storage. Increasing the porosity leads to a progressive decline in cumulative heat storage. The curves primarily cluster based on porosity, with minor variations observed between similar porosity values. Furthermore, under constant porosity, increasing the pore density also reduces the transient heat storage. This degradation is attributed to the suppression of natural convection caused by higher flow resistance in finer pores, which significantly lowers the heat absorption rate. Consequently, the metal foam with a porosity of 0.980 and a pore density of 10 PPI demonstrates the most rapid heat accumulation, achieving the highest energy uptake throughout the melting process.

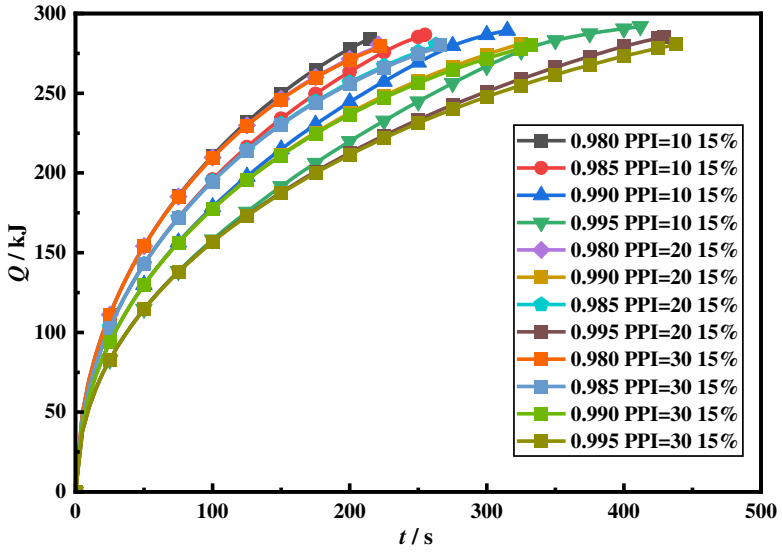

Figure 17: Comparison of transient heat storage under different porosities, pore densities, and nanoparticle additions.

To quantitatively evaluate performance, the average heat storage rate is calculated for twelve structural designs. Fig. 18a compares the total heat storage capacity. The results show that the configuration with the porosity of 0.995, the pore density of 10 PPI, and the nanoparticle concentration of 15% achieves the highest total capacity. This is attributed to its prolonged melting duration and higher final average temperature. However, maximum capacity does not equate to the fastest charging speed. Fig. 18b reveals that the average heat storage rate declines significantly as porosity increases. For the case with a pore density of 10 PPI, increasing porosity from 0.980 to 0.985 reduces the rate from 1.322 to 1.124 kW (a 14.96% drop). A further increase to 0.995 causes a drastic fall to 0.709 kW, representing a 46.37% reduction. In contrast, the impact of pore density is less pronounced. At constant porosity, increasing pore density from 10 PPI to 20 PPI lowers the rate by only 3.92% (from 1.322 to 1.270 kW), and to 30 PPI by 4.65% (to 1.260 kW). Consequently, the optimal design for power density is the tank with the porosity of 0.980, pore density of 10 PPI, and nanoparticle concentration of 15%, achieving a peak average rate of 1.322 kW. Conversely, the slowest performance is observed in the configuration (porosity = 0.995, pore density = 30 PPI), with a power density of 0.641 kW. Comparing these extremes, the fastest design outperforms the slowest by 51.47%, highlighting the critical influence of structural parameters on charging efficiency.

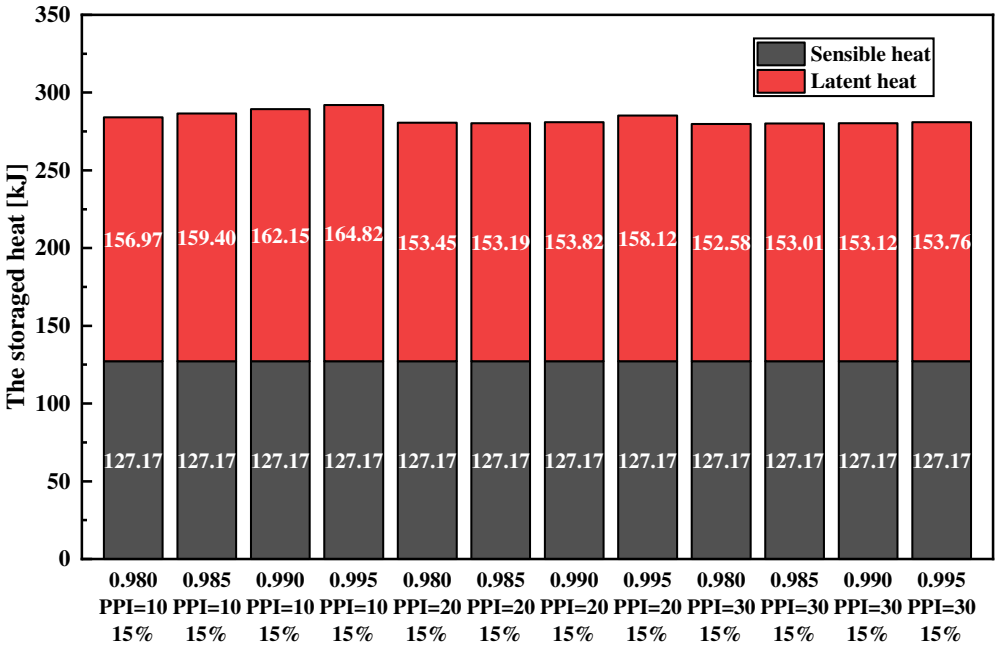

(a)

Figure 18: (Continued)

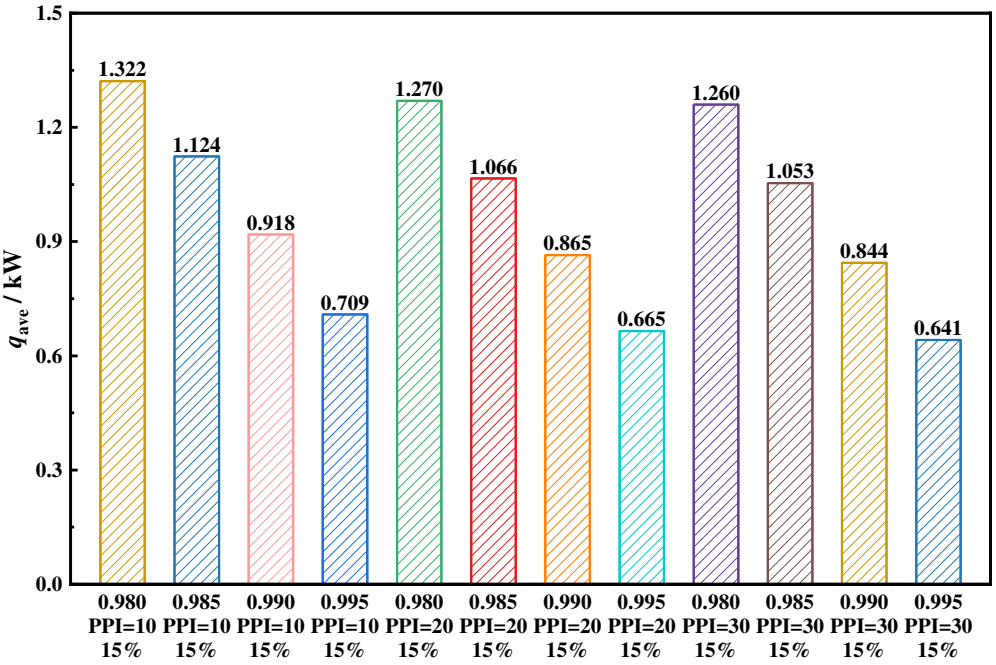

(b)

Figure 18: Comparison of (**a**) total heat storage and (**b**) average heat storage rate under different porosities, pore densities, and nanoparticle additions.

5 Conclusion

This paper investigates the transient solid-liquid phase change in a hybrid that comprises PCM, fin, MF, and nanoparticles. The synergistic influence of the three thermal spreaders has been examined using a well-verified numerical model. A set of numerical simulations have been performed. Based on the comprehensive numerical investigations into the coupled enhancement effects of fin, MF, and nanoparticles on solid-liquid phase change, the following conclusions are drawn:

(1) Porosity is the dominant factor governing the melting rate. Reducing porosity significantly enhances the heat transfer rate and shortens the melting time. Specifically, decreasing porosity from 0.995 to 0.980 reduces the melting time by 53.71%.

(2) Increasing pore density suppresses natural convection, thereby decelerating the melting process. A rise in pore density from 10 PPI to 30 PPI results in a 64.62% decrease in average liquid velocity, extending the complete melting time by 7.78%. This highlights the inherent trade-off between conductive enhancement and convective restriction in metal foam structures.

(3) Nanoparticle addition improves thermal conductivity and accelerates phase change in a concentration-dependent manner. Incorporating nanoparticles up to a 15% concentration reduces the melting time by 25.49%, as the conductive enhancement outweighs the minor suppression of natural convection. Higher concentration consistently improves transient melting fractions and overall energy storage performance.

(4) A synergistic interaction exists between metal foam and nanoparticles, where the enhancement effect of nanoparticles is more pronounced under conditions of weaker intrinsic conduction. The maximum heat transfer enhancement from nanoparticles occurs in metal foam with a porosity of 0.995 and a

pore density of 30 PPI, where the conductive network is the least effective. Consequently, the optimal design in this study achieves a 51.47% higher heat storage rate compared to the worst-case scenario.

These findings provide critical guidance for the multi-parameter design of thermal energy storage systems and underscore the importance of coupled enhancement strategies. While this study considers nanoparticle concentrations up to 15%, achieving such high loadings presents challenges in practical applications due to aggregation. To address this, future engineering implementations should incorporate surfactants to ensure uniform dispersion, thereby enabling higher stable nanoparticle concentrations and maximizing thermal performance.

Acknowledgement: Not applicable.

Funding Statement: The authors received no specific funding for this study.

Author Contributions: The authors confirm contribution to the paper as follows: conceptualization, Rukun Hu, Liao Zhang, Wenbin Han, Wei Chen, Bo Ma, Xuan Liu, Yongzhi Lei, Qian Lu, Yuanji Li and Xiaohu Yang; methodology, Rukun Hu, Liao Zhang and Wenbin Han; software, Wei Chen, Bo Ma and Xuan Liu; validation, Bo Ma, Xuan Liu, Yongzhi Lei and Qian Lu; formal analysis, Yuanji Li and Xiaohu Yang; investigation, Rukun Hu, Liao Zhang, Wenbin Han, Wei Chen, Bo Ma, Xuan Liu, Yongzhi Lei, Qian Lu, Yuanji Li and Xiaohu Yang; resources, Rukun Hu and Liao Zhang; data curation, Xuan Liu and Yongzhi Lei; writing—original draft preparation, Rukun Hu, Liao Zhang, Wenbin Han, Wei Chen, Bo Ma, Xuan Liu, Yongzhi Lei, Qian Lu, Yuanji Li and Xiaohu Yang; writing—review and editing, Rukun Hu and Liao Zhang; visualization, Rukun Hu and Liao Zhang; supervision, Yuanji Li and Xiaohu Yang; project administration, Yuanji Li and Xiaohu Yang. All authors reviewed and approved the final version of the manuscript.

Availability of Data and Materials: Data available on request from the authors.

Ethics Approval: Not applicable.

Conflicts of Interest: The authors declare no conflicts of interest.

References

1. Kartal MT. The role of consumption of energy, fossil sources, nuclear energy, and renewable energy on environmental degradation in top-five carbon producing countries. Renew Energy. 2022;184:871–80. doi:10.1016/j.renene.2021.12.022.
2. Rahman A, Woahid Murad SM, Mohsin AKM, Wang X. Does renewable energy proactively contribute to mitigating carbon emissions in major fossil fuels consuming countries? J Clean Prod. 2024;452:142113. doi:10.1016/j.jclepro.2024.142113.
3. Jaiswal KK, Chowdhury CR, Yadav D, Verma R, Dutta S, Jaiswal KS, et al. Renewable and sustainable clean energy development and impact on social, economic, and environmental health. Energy Nexus. 2022;7:100118. doi:10.1016/j.nexus.2022.100118.
4. Sonyy SM, Chowdhury H, Alam F, Haque N. Methodology for estimating and mitigating intermittency in renewable energy sources. Energy Convers Manage. 2026;350:120943. doi:10.1016/j.enconman.2025.120943.
5. Ekoue MK, Woerman M, Clastres C. Intermittency and uncertainty in wind and solar energy: impacts on the French electricity market. Energy Econ. 2025;142:108176. doi:10.1016/j.eneco.2024.108176.
6. Enasel E, Dumitrascu G. Storage solutions for renewable energy: a review. Energy Nexus. 2025;17:100391. doi:10.1016/j.nexus.2025.100391.
7. Koohi-Fayegh S, Rosen MA. A review of energy storage types, applications and recent developments. J Energy Storage. 2020;27:101047. doi:10.1016/j.est.2019.101047.
8. De Rosa M, Afanaseva O, Fedyukhin AV, Bianco V. Prospects and characteristics of thermal and electrochemical energy storage systems. J Energy Storage. 2021;44:103443. doi:10.1016/j.est.2021.103443.

9. Maruf MNI, Morales-España G, Sijm J, Helistö N, Kiviluoma J. Classification, potential role, and modeling of power-to-heat and thermal energy storage in energy systems: a review. Sustain Energy Technol Assess. 2022;53:102553. doi:10.1016/j.seta.2022.102553.
10. Zhai X, Xu Z, Zhang W, Zhang Q, Yang X, Qu J, et al. Phase change thermal energy storage: materials and heat transfer enhancement methods. J Energy Storage. 2025;123:116778. doi:10.1016/j.est.2025.116778.
11. Duan J, Xiong Y, Yang D. Study on the effect of multiple spiral fins for improved phase change process. Appl Therm Eng. 2020;169:114966. doi:10.1016/j.applthermaleng.2020.114966.
12. Hadadian M, Samiee S, Ahmadzadeh H, et al. Nanofluids for heat transfer enhancement—A review. Phys Chem Res. 2013;1(1):1–33. doi:10.1615/jenhheattransf.2019031575.
13. Li Y, Luo C, Guo J, Wang Q, Yang X, Sundén B. Condensation characteristics on surface with different groove shapes and wettability. Appl Therm Eng. 2025;268:125882. doi:10.1016/j.applthermaleng.2025.125882.
14. Tijing LD, Pak BC, Baek BJ, Lee DH. A study on heat transfer enhancement using straight and twisted internal fin inserts. Int Commun Heat Mass Transf. 2006;33(6):719–26. doi:10.1016/j.icheatmasstransfer.2006.02.006.
15. Zhang S, Mancin S, Pu L. A review and prospective of fin design to improve heat transfer performance of latent thermal energy storage. J Energy Storage. 2023;62:106825. doi:10.1016/j.est.2023.106825.
16. Desalegn GT, Alamnia AT, Belew ML. Innovative fin designs for enhanced thermal performance in PCM-based thermal energy storage: a review. Energy Convers Manag X. 2026;29:101508. doi:10.1016/j.ecmx.2025.101508.
17. Eslami M, Khosravi F, Fallah Kohan HR. Effects of fin parameters on performance of latent heat thermal energy storage systems: a comprehensive review. Sustain Energy Technol Assess. 2021;47:101449. doi:10.1016/j.seta.2021.101449.
18. Diaconu BM, Cruceru M, Anghelescu L. A critical review on heat transfer enhancement techniques in latent heat storage systems based on phase change materials. Passive and active techniques, system designs and optimization. J Energy Storage. 2023;61:106830. doi:10.1016/j.est.2023.106830.
19. Jaberi A, Hossainpour S. Enhanced PCM melting performance in shell and tube latent heat thermal energy storage systems using optimally positioned porous fins. Case Stud Therm Eng. 2025;73:106731. doi:10.1016/j.csite.2025.106731.
20. Kim SH, Pandey S, Park SH, Ha MY. A numerical investigation of the effect of fin inclination angle on the thermal energy storage performance of a phase change material in a rectangular latent heat thermal energy storage unit. J Energy Storage. 2022;47:103957. doi:10.1016/j.est.2022.103957.
21. Abdellatif HE, Ali Khan S, Liu H. Thermal optimization of PCM-based storage systems using L-shaped fins: a numerical and RSM-based approach. Energy. 2025;336:138309. doi:10.1016/j.energy.2025.138309.
22. Ali Khan S, Liu H, Abdellatif HE, Wang Z, Belaadi A, Alhushaybari A. Investigation on enhancing thermal energy storage performance of a phase change material in triplex tube heat exchangers with novel fins configuration. Int Commun Heat Mass Transf. 2025;167:109265. doi:10.1016/j.icheatmasstransfer.2025.109265.
23. Tang S, Song Y, Liu P, Wu X, Xu Y, Zhou J, et al. Design and optimization of a vertical shell-and-tube latent heat thermal energy storage system via discontinuous fins. Renew Energy. 2025;243:122568. doi:10.1016/j.renene.2025.122568.
24. Mohamad AA. Heat transfer enhancements in heat exchangers fitted with porous media Part I: constant wall temperature. Int J Therm Sci. 2003;42(4):385–95. doi:10.1016/S1290-0729(02)00039-X.
25. Xuan Y, Li Q. Heat transfer enhancement of nanofluids. Int J Heat Fluid Flow. 2000;21(1):58–64. doi:10.1016/S0142-727X(99)00067-3.
26. Li Y, Huang X, Yang X, Ai B, Chen S. Comparative study on deep learning prediction of directional thermal conductivity of anisotropic porous media. Int J Therm Sci. 2025;212:109759. doi:10.1016/j.ijthermalsci.2025.109759.
27. Akhavan Mohseni S, Akhavan Mohseni M, Babapoor A, Rahimi-Ahar Z. Application of nano-phase change materials in thermal energy storage: an engineering approach to optimizing efficiency, sustainability, and industrial economics—a review. J Energy Storage. 2025;134:118116. doi:10.1016/j.est.2025.118116.
28. Abdulrazzaq T, Togun H, Reza S, Kazi S, Ariffin M, Adam N. Effect of flow separation of TiO_2 nanofluid on heat transfer in the annular space of two concentric cylinders. Therm Sci. 2020;24(2 Part A):1007–18. doi:10.2298/tsci180709321a.

29. Xiong T, Zheng L, Shah KW. Nano-enhanced phase change materials (NePCMs): a review of numerical simulations. Appl Therm Eng. 2020;178:115492. doi:10.1016/j.applthermaleng.2020.115492.
30. Alhuyi Nazari M, Maleki A, El Haj Assad M, Rosen MA, Haghighi A, Sharabaty H, et al. A review of nanomaterial incorporated phase change materials for solar thermal energy storage. Sol Energy. 2021;228:725–43. doi:10.1016/j.solener.2021.08.051.
31. Daneshazarian R, Antoun S, Dworkin SB. Performance assessment of nano-enhanced phase change material for thermal storage. Int J Heat Mass Transf. 2021;173:121256. doi:10.1016/j.ijheatmasstransfer.2021.121256.
32. Abdolahimoghadam M, Rahimi M. A numerical evaluation of a latent heat thermal energy storage system in the presence of various types of nanoparticles. Appl Therm Eng. 2023;230:120854. doi:10.1016/j.applthermaleng.2023.120854.
33. Sundriyal A, Verma P, Varshney L. Numerical study of the melting rate enhancement of nano phase change material in a modified shell and tube heat exchanger. J Energy Storage. 2024;84:110859. doi:10.1016/j.est.2024.110859.
34. Piroozmand V, Ahmadi R. Enhancement of PCMs performance using nano-particles in horizontal triple-series shell-and-tube heat exchangers: a numerical study. J Energy Storage. 2024;85:111057. doi:10.1016/j.est.2024.111057.
35. Shi J, Du H, Chen Z, Lei S. Review of phase change heat transfer enhancement by metal foam. Appl Therm Eng. 2023;219:119427. doi:10.1016/j.applthermaleng.2022.119427.
36. Aramesh M, Shabani B. Metal foam-phase change material composites for thermal energy storage: a review of performance parameters. Renew Sustain Energy Rev. 2022;155:111919. doi:10.1016/j.rser.2021.111919.
37. Cui W, Si T, Li X, Li X, Lu L, Ma T, et al. Heat transfer enhancement of phase change materials embedded with metal foam for thermal energy storage: a review. Renew Sustain Energy Rev. 2022;169:112912. doi:10.1016/j.rser.2022.112912.
38. Yao Y, Wu H. Thermal transport process of metal foam/paraffin composite (MFPC) with solid-liquid phase change: an experimental study. Appl Therm Eng. 2020;179:115668. doi:10.1016/j.applthermaleng.2020.115668.
39. Buonomo B, Rita Golia M, Manca O, Nardini S. A review on thermal energy storage with phase change materials enhanced by metal foams. Therm Sci Eng Prog. 2024;53:102732. doi:10.1016/j.tsep.2024.102732.
40. Reddy LK, Pujari AK. Multi-objective optimization of metal foam parameters for enhanced performance of LHTES unit in shell-and-tube configurations. Appl Therm Eng. 2025;259:124805. doi:10.1016/j.applthermaleng.2024.124805.
41. Zheng ZJ, Yang C, Xu Y, Cai X. Effect of metal foam with two-dimensional porosity gradient on melting behavior in a rectangular cavity. Renew Energy. 2021;172:802–15. doi:10.1016/j.renene.2021.03.069.
42. Li Y, Xie Y, Gao J, Yang X, Sundén B. Solidification characteristics in rotating gradient metal foam based on Taguchi and response surface analysis. Int J Heat Mass Transf. 2025;250:127324. doi:10.1016/j.ijheatmasstransfer.2025.127324.
43. Liu A, Lin J, Zhuang Y. PIV experimental study on the phase change behavior of phase change material with partial filling of metal foam inside a cavity during melting. Int J Heat Mass Transf. 2022;187:122567. doi:10.1016/j.ijheatmasstransfer.2022.122567.
44. Cheong HJ, Yang JH, Hur JW, Gi HK, Shin JH. Enhancing thermal performance of phase change material with optimized metal foam configuration: experimental and numerical analysis. Appl Therm Eng. 2025;270:126210. doi:10.1016/j.applthermaleng.2025.126210.
45. Pourfallah M, Languri E. Experimental analysis on thermal performance of multi-scale metal foam and PCM composite in a rectangular chamber. Therm Sci Eng Prog. 2025;66:104075. doi:10.1016/j.tsep.2025.104075.
46. Li Y, Huang X, Li Z, Xie Y, Yang X, Li MJ. Structural optimization of latent heat storage tank filled with nickel foam. Appl Therm Eng. 2025;267:125780. doi:10.1016/j.applthermaleng.2025.125780.
47. Ding C, Wang L, Niu Z. Thermal performance evaluation of latent heat storage systems with plate fin-metal foam hybrid structure. Case Stud Therm Eng. 2021;27:101309. doi:10.1016/j.csite.2021.101309.
48. Tahmasbi M, Siavashi M, Karimi AR, Tousi R, Keshtkaran AH. The effects of fins number, metal foam, and helical coil on the thermal storage enhancement of the phase change material: an experimental study. Appl Therm Eng. 2024;253:123780. doi:10.1016/j.applthermaleng.2024.123780.

49. Lu Y, Zuo H, Wu M, Zeng K, Xu H, Kong J, et al. Enhancing the melting performance in latent heat storage systems with fin-foam combination at high temperatures: configurational optimization and economic assessment. Appl Therm Eng. 2024;247:123036. doi:10.1016/j.applthermaleng.2024.123036.
50. Yang B, Zhang R, Gao Z, Yu X. Effect of nanoparticles and metal foams on heat transfer properties of PCMs. Int J Therm Sci. 2022;179:107567. doi:10.1016/j.ijthermalsci.2022.107567.
51. Yang C, Xu Y, Cai X, Zheng ZJ. Melting behavior of the latent heat thermal energy storage unit with fins and graded metal foam. Appl Therm Eng. 2021;198:117462. doi:10.1016/j.applthermaleng.2021.117462.
52. Heyhat MM, Mousavi S, Siavashi M. Battery thermal management with thermal energy storage composites of PCM, metal foam, fin and nanoparticle. J Energy Storage. 2020;28:101235. doi:10.1016/j.est.2020.101235.
53. Fadl M, Eames PC. Numerical investigation of the influence of mushy zone parameter Amush on heat transfer characteristics in vertically and horizontally oriented thermal energy storage systems. Appl Therm Eng. 2019;151:90–9. doi:10.1016/j.applthermaleng.2019.01.102.
54. Calmidi VV, Mahajan RL. Forced convection in high porosity metal foams. J Heat Transf. 2000;122(3):557–65. doi:10.1115/1.1287793.
55. Bhattacharya A, Calmidi VV, Mahajan RL. Thermophysical properties of high porosity metal foams. Int J Heat Mass Transf. 2002;45(5):1017–31. doi:10.1016/S0017-9310(01)00220-4.
56. Boomsma K, Poulikakos D. On the effective thermal conductivity of a three-dimensionally structured fluid-saturated metal foam. Int J Heat Mass Transf. 2001;44(4):827–36. doi:10.1016/S0017-9310(00)00123-X.
57. Žukauskas A. Heat transfer from tubes in crossflow. In: Advances in heat transfer. Vol. 8. Amsterdam: Elsevier; 1972. p. 93–160. doi:10.1016/s0065-2717(08)70038-8.
58. Plautz DA, Johnstone HF. Heat and mass transfer in packed beds. AlChE J. 1955;1(2):193–9. doi:10.1002/aic.690010211.
59. Al-Abidi AA, Mat S, Sopian K, Sulaiman MY, Mohammad AT. Internal and external fin heat transfer enhancement technique for latent heat thermal energy storage in triplex tube heat exchangers. Appl Therm Eng. 2013;53(1):147–56. doi:10.1016/j.applthermaleng.2013.01.011.
60. Zheng H, Wang C, Liu Q, Tian Z, Fan X. Thermal performance of copper foam/paraffin composite phase change material. Energy Convers Manage. 2018;157:372–81. doi:10.1016/j.enconman.2017.12.023.
61. Khodadadi JM, Hosseinizadeh SF. Nanoparticle-enhanced phase change materials (NEPCM) with great potential for improved thermal energy storage. Int Commun Heat Mass Transf. 2007;34(5):534–43. doi:10.1016/j.icheatmasstransfer.2007.02.005.
62. Mhiri H, Jemni A, Sammouda H. Numerical and experimental investigations of melting process of composite material (nanoPCM/carbon foam) used for thermal energy storage. J Energy Storage. 2020;29:101167. doi:10.1016/j.est.2019.101167.